 CMES, vol.91, no.5, pp.355-376, 2013

Dam-break model with Characteristic-Based Operator-Splitting Finite Element Method

Da-guo Wang[1,2] and Leslie-George Tham[2] and Qing-xiang Shui[1]

Abstract: A finite element method, which is the characteristic-based operator-splitting (CBOS) algorithm, is adopted to solve unsteady incompressible Navier-Stokes (N-S) equations. In each time step, the equations are split into the diffusive part and the convective part. The convective part is discretized using the characteristic Galerkin method and solved explicitly. The moving interface is captured by the pseudo-concentration method, thus, a new dam-break model is established. Through the validation of a dam-break onto a downstream dry bed or wet bed, it is shown that the present model can accurately simulate the moving interface flows. We also study dam-break in a confined reservoir and the dam-break wave impact on a spur dike. The complexity of the interface shape occurring in the different stages, including the gradual formation of the air bubble in the case of dam-break in a confined reservoir, and the generation of dam-break wave, the overtopping the spur dike and the impacting on the downstream seabed in the case of the dam-break wave impact on a spur dike, can be obtained.

Keywords: characteristic-based operator-splitting finite element method, N-S equations, pseudo-concentration method, dam-break

1 Introduction

Dam-break flows are an important practical problem in civil engineering and their prediction is a required element in the design of a dam and its surrounding environment. There are two common approaches, namely Shallow Water approach and Navier-Stokes (N-S) approach, to solve the dam-break problem. Numerical simulation of the N-S approach is complex, since it involves the solution of the unsteady incompressible N-S equations coupled with the moving interface tracking.

[1] School of Environment and Resource, Southwest University of Science and Technology, Mianyang 621010, China

[2] Department of Civil and Structural Engineering,The University of Hong Kong, Hong Kong 999077, China

There are commonly-used three numerical methods to solve the unsteady incompressible N-S equations, i.e., finite difference method (FDM) [Douglas and Russell (1982)], finite volume method (FVM) [Boivin, Cayré, and Hérard (2000); Kami and Ossowski (2011)] and finite element method (FEM). The FEM is widely used for its good ability in dealing with complex geometric boundaries and various finite element methods have been developed. The traditional Galerkin finite element scheme is equivalent to the central difference. With the increase of Reynolds number, the convective term in the N-S equations gradually becomes more dominant. It exhibits strong nonlinear characteristics, which leads to the distortion and oscillation of numerical solutions. In order to overcome the above difficulties, many efforts have been devoted to develop stabilized methods, which include Petrov-Galerkin (P-G) method [Christie, Griffiths, Mitchell, and Zienkiewicz (1976)], least square finite element method [Hughes, Franca, and Hulbert (1989)], Taylor-Galerkin (T-G) method [Donea (1984)], characteristic-based-split (CBS) algorithm [Zienkiewicz, Nithiarasu, Codina, Vázquez, and Ortiz (1999)] and characteristic-based operator-splitting (CBOS) algorithm [Wang, Wang, Xiong, and Tham (2011)]. The CBOS algorithm, which combined the advantages of the CBS algorithm and the operator-splitting algorithm, split the N-S equations into the diffusive part and the convective part within each time step by adopting operator-splitting technique. Both the convection dominated characteristics and diffusive property are considered by solving the two parts separately. The simple explicit characteristic time discretization, which involves a local Taylor expansion, is referenced from the CBS algorithm and applied to the discretization of the convective part. An additional steady streamline diffusion term is given by the discretization equation along the characteristic. It differs from the previous methods in which the weight function is modified by artificial or empirical factor. Thus the difficulty of choosing weight functions in P-G method or other finite element methods is avoided.

Meanwhile, there are a lot of numerical methods advocated for solving moving interface problems. They might be classified into two categories: interface tracking approach [Hirt, Cook, and Butler (1970); Masud and Hughes (1997)] and interface capturing approach. In the interface capturing approach, the mesh remains fixed and the moving interface can not be directly defined by the mesh nodes. Therefore, additional technique is necessary to define the areas occupied by fluid or gas on either side of the interface. The marker-and-cell (MAC) method [Harlow and Welch (1965)], the volume of fluid (VOF) method [Hirt and Nichlos (1981); Park, Kim, Kim, and Van (2012)], the level set method (LSM) [Osher and Sethian (1988)] and the pseudo-concentration method (PCM) [Kačeniauskas (2008); Aliabadi and Tezduyar (2000)] are well known methods using the interface capturing approach. In the PCM, it uses a pseudo-concentration function defined in the entire domain and

solves directly a hyperbolic equation to determine the moving interface. Sometimes pseudo-concentration function is chosen to be very close to volume fraction function widely used in the VOF method and finite volumes. In the most cases the PCM is more efficient than the LSM, because it uses simpler front reconstruction techniques [Kačeniauskas (2008); Aliabadi and Tezduyar (2000)].

A new dam-break model, in which the CBOS algorithm is used to solve the N-S equations and the PCM is used to capture the moving interface, is established. The dam-break onto a downstream dry bed or wet bed is adopted to validate the present model. In addition, we study the dam-break in a confined reservoir and the dam-break wave impact on a spur dike. In Section 2, the governing equations are illustrated. The numerical methods and finite element solutions are discussed in Section 3. In Section 4, the surface tracking is described and the solution procedure is reported in Section 5. The model verification and the model application are carried out in Section 6 and in Section 7 respectively.

2 Governing equations

The two-dimensional unsteady viscous incompressible flows can be governed by the N-S equations and theirs forms are expressed as

$$\frac{\partial u_i}{\partial x_i} = 0 \tag{1}$$

$$\rho \frac{\partial u_i}{\partial t} + \rho u_j \frac{\partial u_i}{\partial x_j} = -\frac{\partial p}{\partial x_i} + \mu \frac{\partial}{\partial x_j}\left(\frac{\partial u_i}{\partial x_j} + \frac{\partial u_j}{\partial x_i}\right) + \rho f_i, \tag{2}$$

where $i, j = 1, 2$, x_i is the Cartesian coordinates, u_i is the velocity components in x_i direction, p is the pressure, t is the time, μ is the dynamic viscosity coefficient, ρ is the density of the fluid, f_1 is the external force in horizontal direction and f_2 is the external force in vertical direction.

3 Numerical methods and finite element solutions

3.1 Operator-splitting algorithm

By adopting the operator-splitting algorithm, the governing equations (1) and (2) are split into the diffusive part

$$\begin{cases} \rho \frac{\partial u_i^{n+\theta}}{\partial t} - \mu \frac{\partial}{\partial x_j}\left(\frac{\partial u_i^{n+\theta}}{\partial x_j} + \frac{\partial u_j^{n+\theta}}{\partial x_i}\right) = -\frac{\partial p^{n+1}}{\partial x_i} + \rho f_i, \\ \frac{\partial u_i^{n+\theta}}{\partial x_i} = 0 \end{cases} \tag{3}$$

and the convective part

$$\frac{\partial u_i^{n+1}}{\partial t} + u_j^{n+1}\frac{\partial u_i^{n+1}}{\partial x_j} = 0, \tag{4}$$

where $u_i^{n+\theta}$ is the solution of the diffusive part (3) at the $n+1$th time step and is also the initial value of the convective part (4) at the $n+1$th time step, u_i^{n+1} is the solution of the convective part (4) at the $n+1$th time step and is also the solution of the N-S equations (1)-(2) at the $n+1$th time step.

3.2 Characteristic method of the convective term

The one-dimensional scalar convection equation can be written as

$$\frac{\partial \phi}{\partial t} + u\frac{\partial \phi}{\partial x} = 0 \tag{5}$$

The characteristic formula of Eq. (5) is

$$\frac{dx}{dt} = u \tag{6}$$

Let

$$x^{'} = x - ut \tag{7}$$

Taking the differentiation of Eq. (7) gives

$$dx^{'} = dx - udt \tag{8}$$

Nothing $\phi = \phi(x^{'}, t)$, we have

$$\left.\frac{\partial \phi}{\partial t}\right|_{x\text{const}} = \frac{\partial \phi}{\partial x^{'}}\frac{\partial x^{'}}{\partial t} + \left.\frac{\partial \phi}{\partial t}\right|_{x^{'}\text{const}} = -u\frac{\partial \phi}{\partial x^{'}} + \left.\frac{\partial \phi}{\partial t}\right|_{x^{'}\text{const}} \tag{9}$$

Along the characteristic, the convective equation can be written as

$$\frac{\partial \phi[x^{'}(t), t]}{\partial t} = 0. \tag{10}$$

So, ϕ is consistent with the characteristic

$$\phi^{n+1} = \phi^n|_{x-\delta} = \phi^n - \delta\frac{\partial \phi^n}{\partial x} + \frac{\delta^2}{2}\frac{\partial^2 \phi^n}{\partial x^2} + o(\Delta t^3) \tag{11}$$

where $\delta = \bar{u}\Delta t$, $\bar{u}$ is the averaged value of u along the characteristic, Δt is the time step. Approximating $\bar{u}$, we can obtain

$$\bar{u} = \frac{u^{n+1} + u^n|_{x-\delta}}{2} \tag{12}$$

Through the Taylor expansion, we have

$$u^n|_{x-\delta} = u^n - \Delta t u^n \frac{\partial u^n}{\partial x} + o(\Delta t^2) \tag{13}$$

Substituting Eq. (13) into Eq. (12) gives

$$\delta = \Delta t u^{n+1/2} - \frac{\Delta t^2}{2} u^n \frac{\partial u^n}{\partial x} \tag{14}$$

where $u^{n+1/2} = \frac{u^{n+1}+u^n}{2}$. Inserting the δ into Eq. (11), we get

$$\phi^{n+1} - \phi^n = -(\Delta t u^{n+1/2} - \frac{\Delta t^2}{2} u^n \frac{\partial u^n}{\partial x}) \frac{\partial \phi^n}{\partial x} + \frac{(\Delta t u^{n+1/2} - \frac{\Delta t^2}{2} u^n \frac{\partial u^n}{\partial x})^2}{2} \frac{\partial^2 \phi^n}{\partial x^2} \tag{15}$$

In order to obtain a fully explicit scheme, $u^{n+1/2}$ can be approximated as

$$u^{n+1/2} = u^n - \frac{\Delta t}{2} u^n \frac{\partial u^n}{\partial x} + o(\Delta t^2). \tag{16}$$

Substituting Eq. (16) into Eq. (15) and ignoring all higher-order terms gives

$$\phi^{n+1} - \phi^n = -\Delta t u^n \frac{\partial \phi^n}{\partial x} + \Delta t^2 u^n \frac{\partial}{\partial x} \left(u^n \frac{\partial \phi^n}{\partial x} \right). \tag{17}$$

Extending Eq. (17) to the two-dimensional nonlinear convective equation, we obtain the temporal discretization of the convective part as

$$u_i^{n+1} - u_i^n = -\Delta t u_j^n \frac{\partial u_i^n}{\partial x_j} + \Delta t^2 u_k^n \frac{\partial}{\partial x_k} \left(u_j^n \frac{\partial u_i^n}{\partial x_j} \right), \tag{18}$$

where $k = 1, 2$. The last term in Eq. (18) is the steady diffusive term along the streamline, which is directly derived from the convective equation.

3.3 Finite element solutions

3.3.1 Finite element solutions for the diffusive part

The temporal discretization of the diffusive part (3) is performed by the backward difference method. Omitting the superscript of p and taking $u_i^{n+\theta}$ as u_i, we have

$$\rho \frac{u_i - u_i^n}{\Delta t} - \mu \frac{\partial}{\partial x_j} \left(\frac{\partial u_i}{\partial x_j} + \frac{\partial u_j}{\partial x_i} \right) = -\frac{\partial p}{\partial x_i} + \rho f_i. \tag{19}$$

We take each element as quadrilateral with 9-nodes where all nine nodes are associated with velocities and only corner nodes with pressures. Employing the standard Galerkin method, the spatial discretization of Eq. (19) can be obtained

$$\begin{aligned}
&\rho u_{i\beta}\iint_{\Omega} N_\beta N_\alpha \, d\Omega + \Delta t\mu u_{i\beta}\iint_{\Omega}\left(\frac{\partial N_\beta}{\partial x_j}+\frac{\partial N_\beta}{\partial x_i}\delta_{ij}\right)\frac{\partial N_\alpha}{\partial x_j}\, d\Omega \\
&- u_{i\beta}\iint_{\Omega}\frac{\partial N_\beta}{\partial x_i}M_l\, d\Omega - \Delta t\, p_l\iint_{\Omega} M_l\frac{\partial N_\alpha}{\partial x_i}\, d\Omega \\
&= \Delta t\mu\iint_{\Gamma}\frac{\partial u_i}{\partial n}N_\alpha\, d\Gamma + \Delta t\rho\iint_{\Omega} f_i N_\alpha\, d\Omega - \Delta t\iint_{\Gamma} n_i p M_l N_\alpha\, d\Gamma + \rho u^n_{i\beta}\iint_{\Omega} N_\beta N_\alpha\, d\Omega
\end{aligned} \tag{20}$$

where N_α, N_β are the quadratic interpolation function, M_l is the linear interpolation function, $\alpha = 1,2,\ldots,m$, $\beta = 1,2,\ldots,m$, $l = 1,2,\ldots,h$, m is the number of velocity nodes of basic element and $m = 9$, h is the number of pressure nodes of basic element and $h = 4$, δ_{ij} is the permutation operator, $\delta_{ij}u_{i\beta} = u_{j\beta}$. The pressure p^{n+1} and velocities $u_i^{n+\theta}$ can be obtained from Eq. (20).

3.3.2 Finite element solutions for the convective part

Similar to the diffusive part, the weak form of Eq. (18) is established by the standard Galerkin method as follows

$$\iint_{\Omega}(u_i^{n+1}-u_i)\delta u_i\, d\Omega = -\Delta t\iint_{\Omega} u_j\frac{\partial u_i}{\partial x_j}\delta u_i\, d\Omega + \Delta t^2\iint_{\Omega} u_k\frac{\partial}{\partial x_k}\left(u_j\frac{\partial u_i}{\partial x_j}\right)\delta u_i\, d\Omega \tag{21}$$

Integrating the last term in the left of Eq. (21) by the partial integration method and ignoring the influence of boundary item gives

$$\iint_{\Omega}(u_i^{n+1}-u_i)\delta u_i\, d\Omega = -\Delta t\iint_{\Omega} u_j\frac{\partial u_i}{\partial x_j}\delta u_i\, d\Omega - \Delta t^2\iint_{\Omega} u_j\frac{\partial u_i}{\partial u_j}u_k\frac{\partial \delta u_i}{\partial x_k}\, d\Omega \tag{22}$$

From Eq. (23), we have

$$\begin{aligned}
&u^{n+1}_{i\beta}\iint_{\Omega} N_\alpha N_\beta\, d\Omega = u_{i\beta}\iint_{\Omega} N_\alpha N_\beta\, d\Omega - u_{j\gamma}u_{i\beta}\Delta t\iint_{\Omega} N_\gamma\frac{\partial N_\beta}{\partial x_j}N_\alpha\, d\Omega \\
&- u_{j\eta}u_{i\gamma}u_{k\beta}\Delta t^2\iint_{\Omega} N_\eta\frac{\partial N_\gamma}{\partial x_j}N_\beta\frac{\partial N_\alpha}{\partial x_k}\, d\Omega
\end{aligned} \tag{23}$$

where N_γ and N_η are the quadratic interpolation function, $\gamma,\eta = 1,2,\ldots,m$. The velocities u_i^{n+1} can be derived from Eq. (23).

4 Surface tracking

The propagation of the moving interface is described by the PCM [Kačeniauskas (2008); Aliabadi and Tezduyar (2000)] based on the interface capturing approach. The evolution of the interface is governed by the time dependent convection equation

$$\frac{\partial C}{\partial t} + \mathbf{u} \cdot \nabla C = 0 \tag{24}$$

where C is the pseudo-concentration function serving as a marker identifying water A and air B with densities ρ_A and ρ_B and viscosities μ_A and μ_B. Thus, in the N-S Eqs. (1)-(2), the density and the viscosity are defined as

$$\rho = C\rho_A + (1-C)\rho_B, \tag{25}$$

$$\mu = C\mu_A + (1-C)\mu_B. \tag{26}$$

$C = 1$ for water A and $C = 0$ for air B. The initial conditions defined on the entire solution domain should be prescribed for the Eq. (24).

The solution of Eq. (24) is the same as that of the convective part (4) and it can be discretized using the characteristic Galerkin method.

5 Solution procedure

(1) The density and the viscosity in the N-S Eqs. (1)-(2) can be obtained by solving Eqs. (25)-(26).

(2) Solve the diffusive part (3) to obtain $u_i^{n+\theta}$ and p^{n+1}.

(3) Take $u_i^{n+\theta}$ as the initial value of the convective part (4) and solve the convective part (4) to get u_i^{n+1}.

(4) Solve Eq. (24) to gain C^{n+1}.

(5) Progress with a time step and go back to step 1.

6 Model verification

Dam-break onto a downstream dry bed or a wet bed is used to validate the dam-break model. In all the cases, including the following Section 7, the fluids involved are water, with $\rho_A = 1000kg/m^3$ and $\mu_A = 10^{-2}Pa \cdot S$, and air, with $\rho_B = 1kg/m^3$ and $\mu_B = 10^{-4}Pa \cdot S$. For convenience, dimensionless length, time and pressure are defined as

$$x^* = x/H, \tag{27}$$

$$y^* = y/H, \tag{28}$$

$$t^* = t\sqrt{g/H}, \tag{29}$$

$$p^* = p/\rho_A g H, \tag{30}$$

where H is the upstream water level height and g is the gravity acceleration.

6.1 Dam-break onto a dry bed

Fig. 1 depicts the problem lay-out and the mesh. All boundaries are considered as impermeable and frictionless walls. A pressure datum is set at the upper right hand corner, where the pressure is set to zero. The computational domain is divided into 128×48 quadrilateral elements.

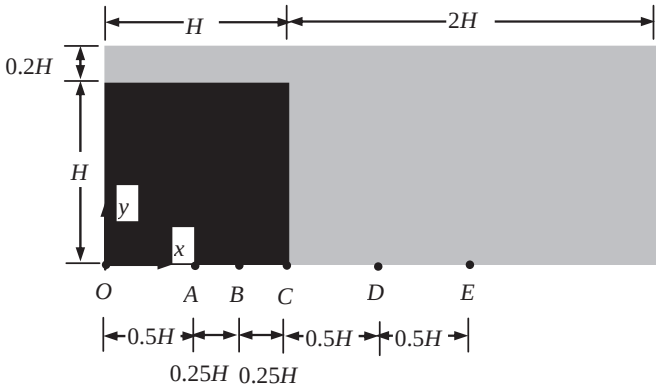

(a) Problem lay-out (where H is the upstream water level height and $H = 0.05175\text{m}$)

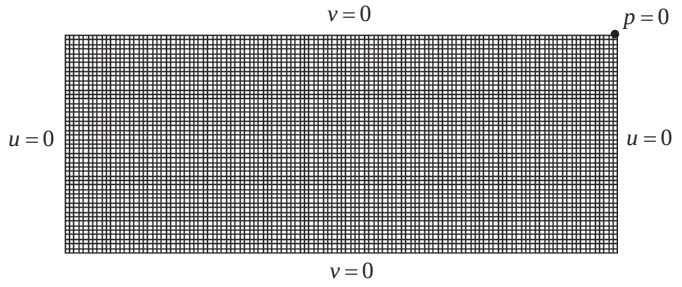

(b) Mesh and boundary conditions

Figure 1: Dam-break on a dry bed case

Fig. 2 shows the position of the water wave front and the height of the residual water column as functions of elapsed time. Good agreement with the experimental data and the other computational results indicates that the present model is capable of predicting the collapse of water column accurately. In order to illustrate the evolution of the free surface, Fig. 3 shows the free surfaces at different instant. The water column starts to collapse from the upper right. The water wave then accelerates rapidly along the floor in the right direction as time elapses.

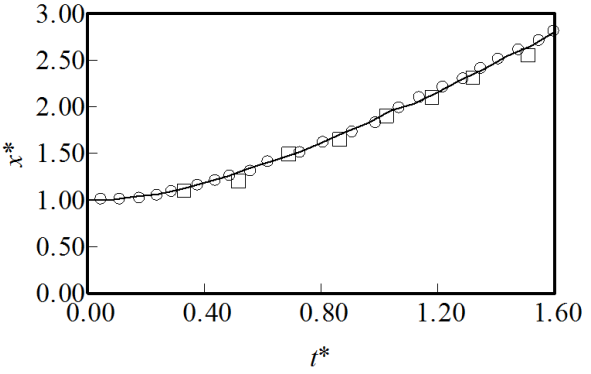

(a) Position of the water wave front

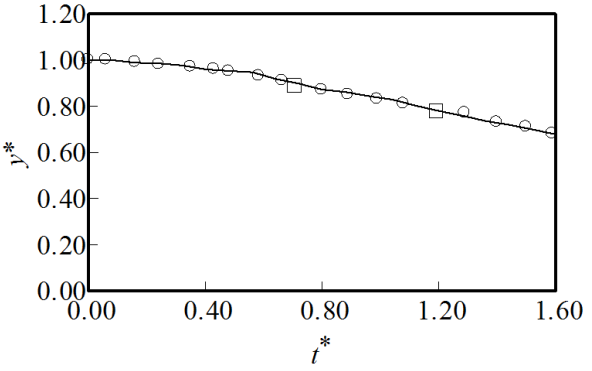

(b) Height of the residual water column

Figure 2: Position of the water wave front and height of the residual water column as functions of time (where solid lines are the results of the present model, round dot markers are the results in [Kim and Lee (2003)] and quadrate dot markers are the results in [Martin and Moyce (1952)])

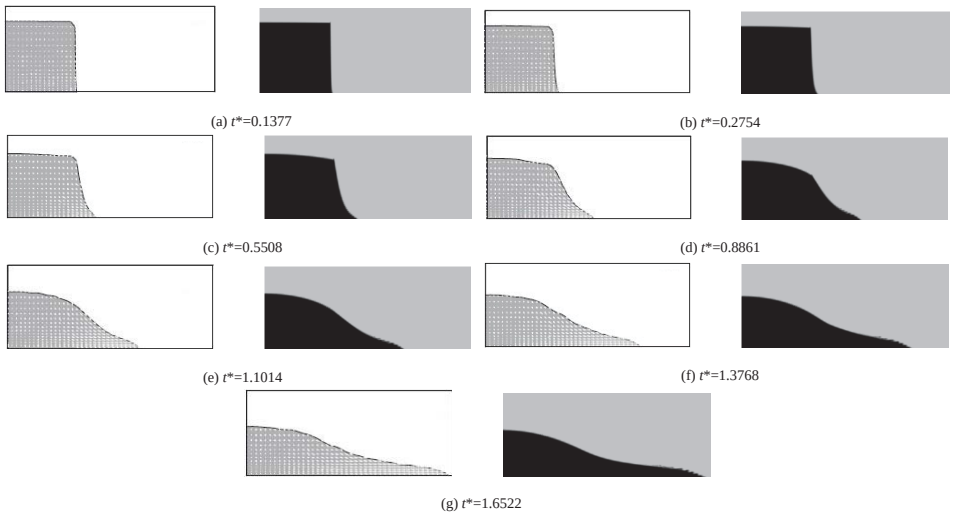

Figure 3: Free surface profiles at different instant on a dry bed case (Left: results in [Kim and Lee (2003)]; right: results of the present model)

Fig. 4 plots the pressure history at the control points indicated in Fig. 1. The pressure near the dam site doesn't satisfy the hydrostatic pressure. It starts increasing as the water starts flowing in the downstream direction. Later on, it decreases. Finally, as time evolves, it approaches the hydrostatic value. This is agreement with that found in [Quecedo, Pastor, Herreros, Merodo, and Zhang (2005)] adopted N-S equations.

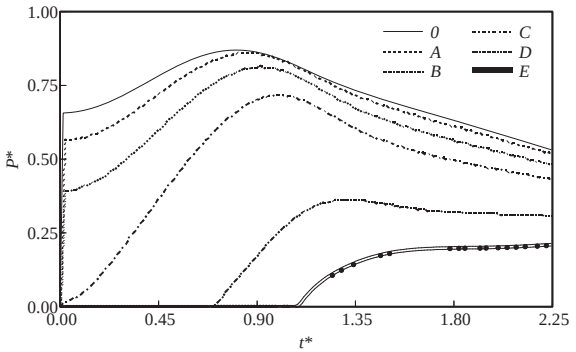

Figure 4: Evolution of the pressure at the control points (Location of the control points shown in Fig. 1)

6.2 Dam-break onto a wet bed

Fig. 5 presents the problem lay-out and the mesh. All boundaries are considered as impermeable and frictionless walls. A pressure datum is set at the upper right hand corner, where the pressure is set to zero. The computational domain is divided into $180 \times (40+5)$ quadrilateral elements.

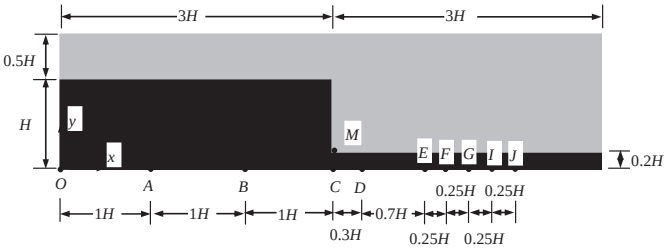

(a) Problem lay-out (where H is the upstream water level height and $H = 0.1\text{m}$)

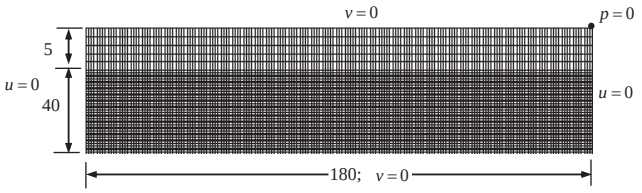

(b) Mesh and boundary conditions

Figure 5: Dam-break on a wet bed case

Fig. 6 depicts the evolution of the surface after dam failure. At the initial instant after failure, the vertical and horizontal velocities at the point M (Shown in Fig. 5) are of the same order of magnitude, so it will produce the upper-right surge wave (Shown in Figs. 6(a-d)). Later on, the vertical velocity becomes progressively minor compared to the horizontal component, but the height of the surge wave increases constantly (Shown in Figs. 6(e-f)). As time passes, the vertical velocity is almost zero, the height of the surge wave hardly increases (Shown in Figs. 6(g-p)). Around $t^* = 1.287$, under gravity, the front of the surge wave begins to move downward and a curved surface is gradually formed. At $t^* = 2.2572$, the front impacts on the water of the downstream wet bed. This result is also found in [Quecedo, Pastor, Herreros, Merodo, and Zhang (2005)] adopted the N-S equations. Meanwhile, at the initial time of failure, the water wave front of the present model is behind the one of the Shallow Water approach (Shown in Fig. 6(h)), but as time elapses, the difference reduces to become negligible (Shown in Fig. 6(p)), which results from

the hydrostatic pressure distribution assumed by the Shallow Water approach. This is agreement with that found in [Quecedo, Pastor, Herreros, Merodo, and Zhang (2005)] and in [Mohapatra, Eswaran, and Bhallamudi (1999)].

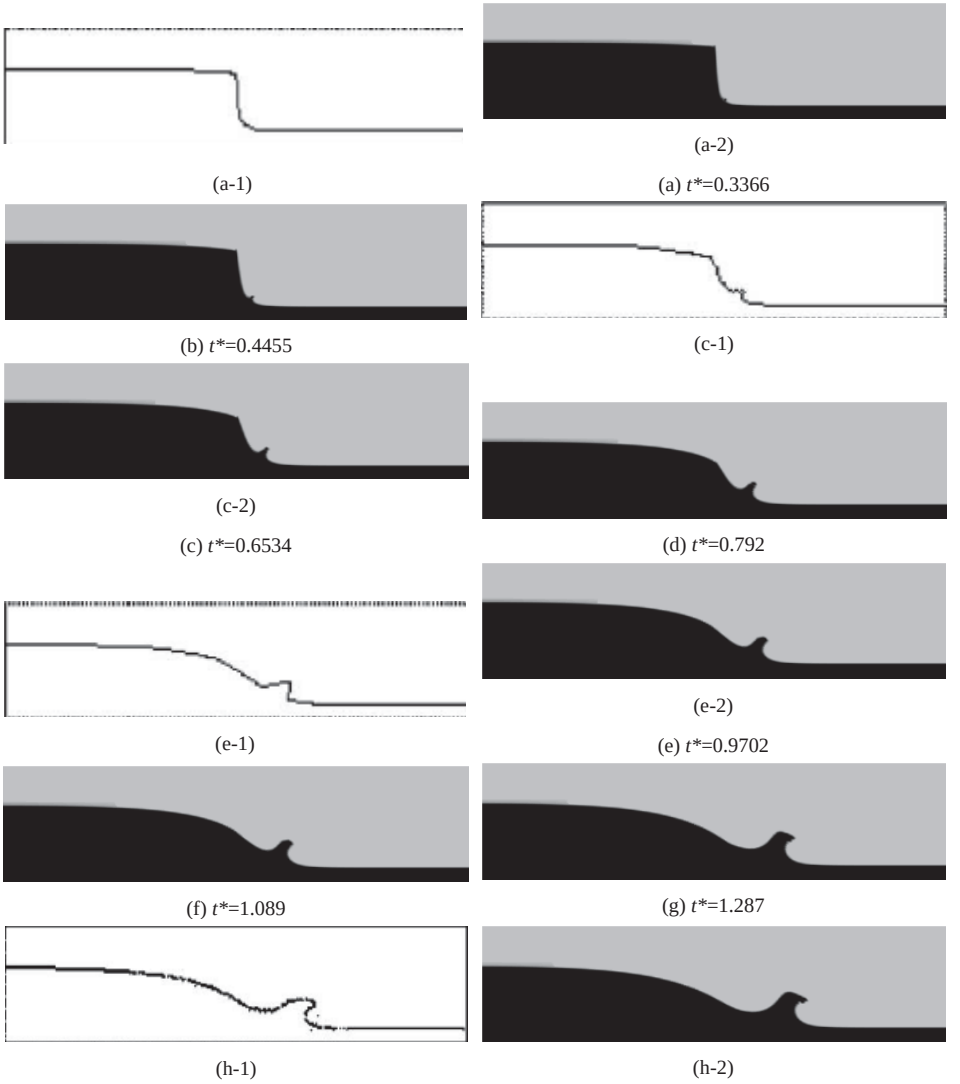

(a-1) (a-2)

(a) t^*=0.3366

(b) t^*=0.4455 (c-1)

(c-2)

(c) t^*=0.6534 (d) t^*=0.792

(e-1) (e-2)

(e) t^*=0.9702

(f) t^*=1.089 (g) t^*=1.287

(h-1) (h-2)

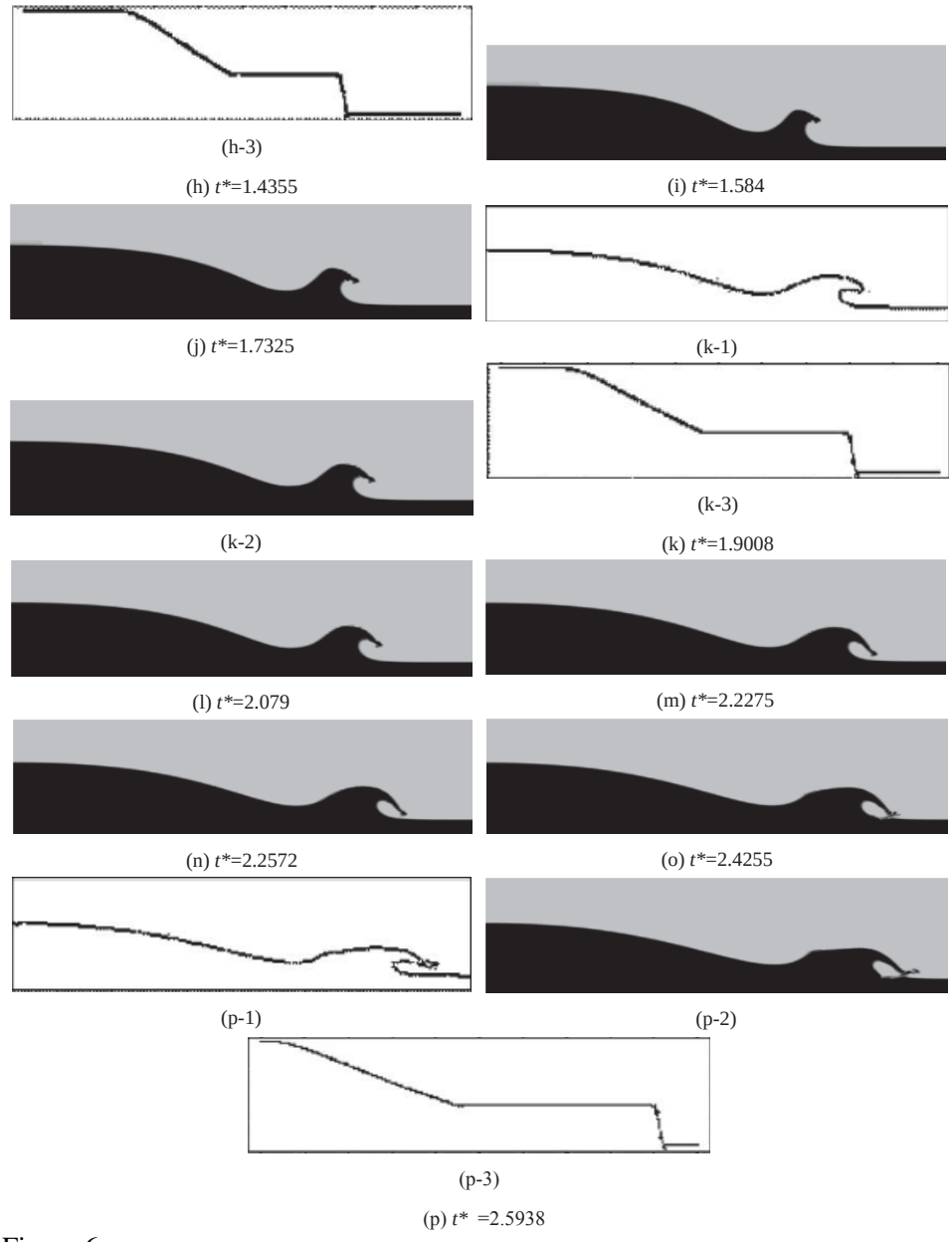

Figure 6: Free surface profiles on a wet bed case (where Figs. (a-2), (b), (c-2), (d), (e-2), (f), (g), (h-2), (i), (j), (k-2), (l), (m), (n), (o) and (p-2) are the results of the present model; Figs. (a-1), (c-1), (e-1), (h-1), (k-1) and (p-1) are the results in [Quecedo, Pastor, Herreros, Merodo and Zhang (2005)] adopted the N-S equations; Figs. (h-3), (k-3), (p-3) are the results in [Quecedo, Pastor, Herreros, Merodo, and Zhang (2005)] adopted the Shallow Water equations)

Fig. 7 depicts the evolution of the pressure at the ten control points indicated in Fig. 5. It should be pointed out that the pressure of the downstream bed suddenly increases while the front of the surge wave impacts on the downstream wet bed.

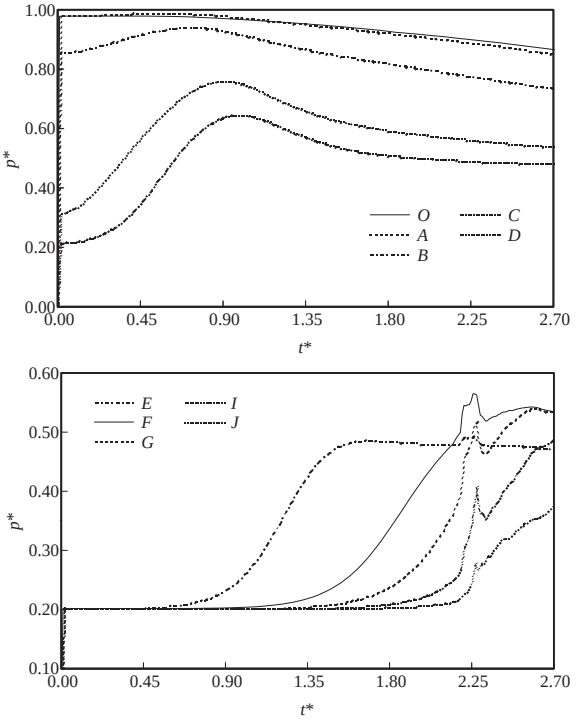

Figure 7: Evolution of the pressure at the control points (Location of the control points shown in Fig. 5)

7 Model application

7.1 Dam-break in a confined reservoir

Fig. 8 presents the problem lay-out and the mesh. No-slip boundary condition is imposed on the top wall, and the other sides are slip boundary conditions. A pressure datum is set at the upper right hand corner, where the pressure is set to zero. The computational domain is divided into 120×40 quadrilateral elements.

Fig. 9 shows the time evolution of the surface after dam failure in a confined reservoir. The complexity of the interface shape occurring in the different stages can be easily captured. Figs. 9(c), 9(d), 9(e) illustrate the behaviour of the flow in the right

corner at the top wall. The backward moving wave fold gradually over and a small amount of air is trapped in Figs. 9(f), 9(g), 9(h), 9(i), 9(j), 9(k) and 9(l). Figs. 9(j), 9(k) and 9(l) depict that another small amount of air is gradually trapped.

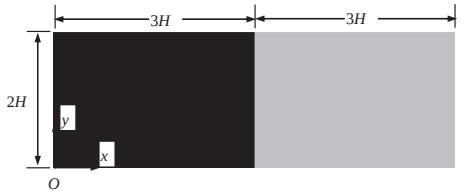

(a) Problem lay-out (H is the upstream water level height and $H = 0.015\text{m}$)

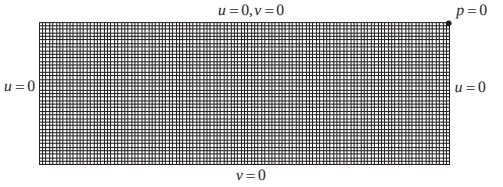

(b) Mesh and boundary conditions

Figure 8: Dam-break in a confined reservoir

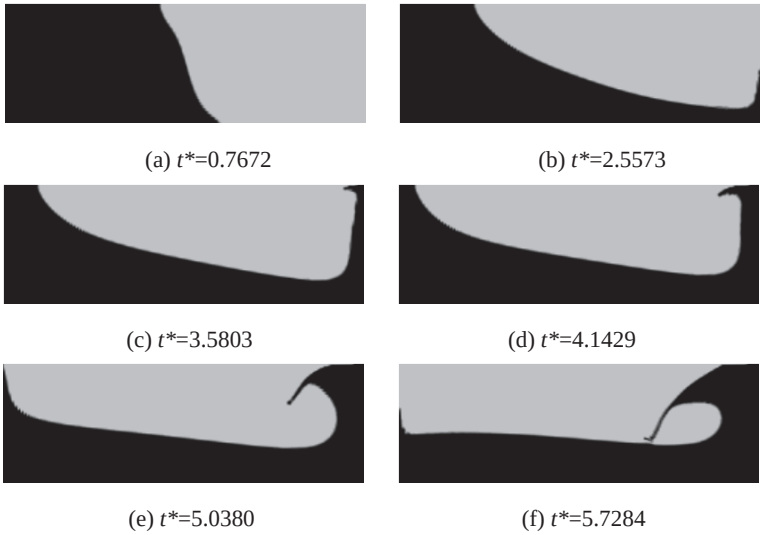

(a) t^*=0.7672 (b) t^*=2.5573

(c) t^*=3.5803 (d) t^*=4.1429

(e) t^*=5.0380 (f) t^*=5.7284

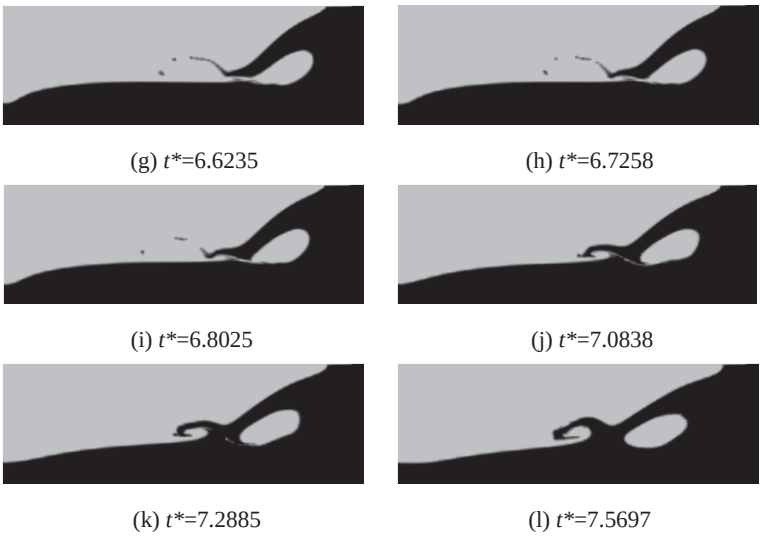

(g) t^*=6.6235 (h) t^*=6.7258

(i) t^*=6.8025 (j) t^*=7.0838

(k) t^*=7.2885 (l) t^*=7.5697

Figure 9: Free surface profiles in a confined reservoir (where t^* is dimensionless time and defined in Eq. (29))

7.2 Dam-break wave impact on a spur dike

Dam-break wave has a powerful impact on the downstream dam and seriously threaten the safety of the downstream dam. In the paper, the dam is assumed as a rigid spur dike and the downstream bed is considered initially dry. Fig. 10 depicts the problem lay-out and the mesh. All boundaries, including the top and the sides of the spur dike, are considered impermeable and frictionless walls. A pressure datum is set at the upper right hand corner, where the pressure is set to zero. The computational domain is divided into 6436 quadrilateral elements, and the length and the width of each element is $H_3/16$. For convenience, dimensionless length, time and pressure are defined as

$$x^* = x/H_3 = 50x, \tag{31}$$

$$y^* = y/H_3 = 50y, \tag{32}$$

$$t^* = t\sqrt{g/H_3} = 22.15t, \tag{33}$$

$$p^* = p/\rho_A g H_3 = 0.005p. \tag{34}$$

Fig. 11 depicts the free surfaces at different instant. Figs. 11(a), 11(b) and 11(c) illustrate the generation of the dam-break wave. The dam-break wave overtopping the spur dike is shown in Figs. 11(d), 11(e), 11(f) and 11(g). Figs. 11(h) and 11(i)

represent the wave impinging on downstream seabed. Fig. 12 depicts the evolution of the pressure calculated at the control points indicated in Fig. 10. The pressures, including acting on the downstream seabed and the spur dike, suddenly increase under the dam-break wave over the spur dike impacting on the downstream seabed. In addition, it should be pointed out that at point located at the top of the spur dike, the pressure decreases even up to negative values, which may be the reason that the center of curvature of the free surface is below the free surface in [Quecedo, Pastor, Herreros, Merodo, and Zhang (2005)].

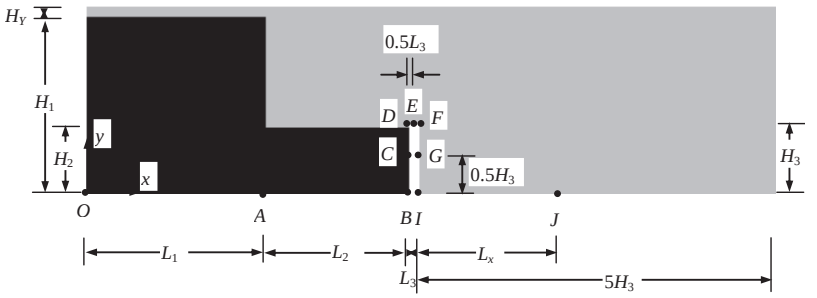

(a) Problem lay-out

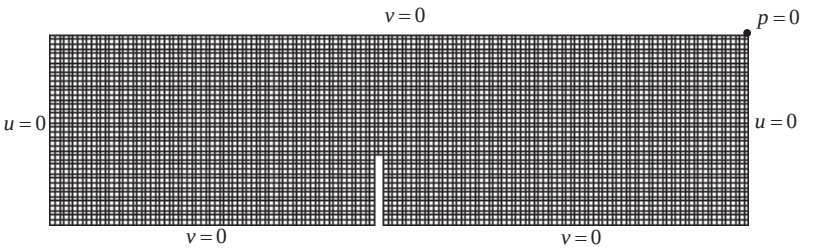

(b) Mesh and boundary conditions

Figure 10: Dam-break wave impact on a spur dike (where H_3 is the height of spur dike and $H_3 = 0.02m$, H_1 is the upstream water level height and $H_1/H_3 = 2.5$, and $H_Y + H_1 = 2.625H_3$, H_2 is the water level height between the failure dam site and the spur dike and $H_2 = 0.9375H_3$, L_1 the length of the upstream riverbed and $L_1 = 2.5H_3$, L_2 is the length between the failure dam site and the spur dike and $L_2 = 2.0H_3$, L_3 is the width of the spur dike and $L_3 = 0.125H_3$, L_x is the length between point J and the spur dike and $L_x = 1.625H_3$ in the case of the paper, and the J is the maximum pressure point that dam-break wave overtopping the spur dike impacts on the downstream riverbed)

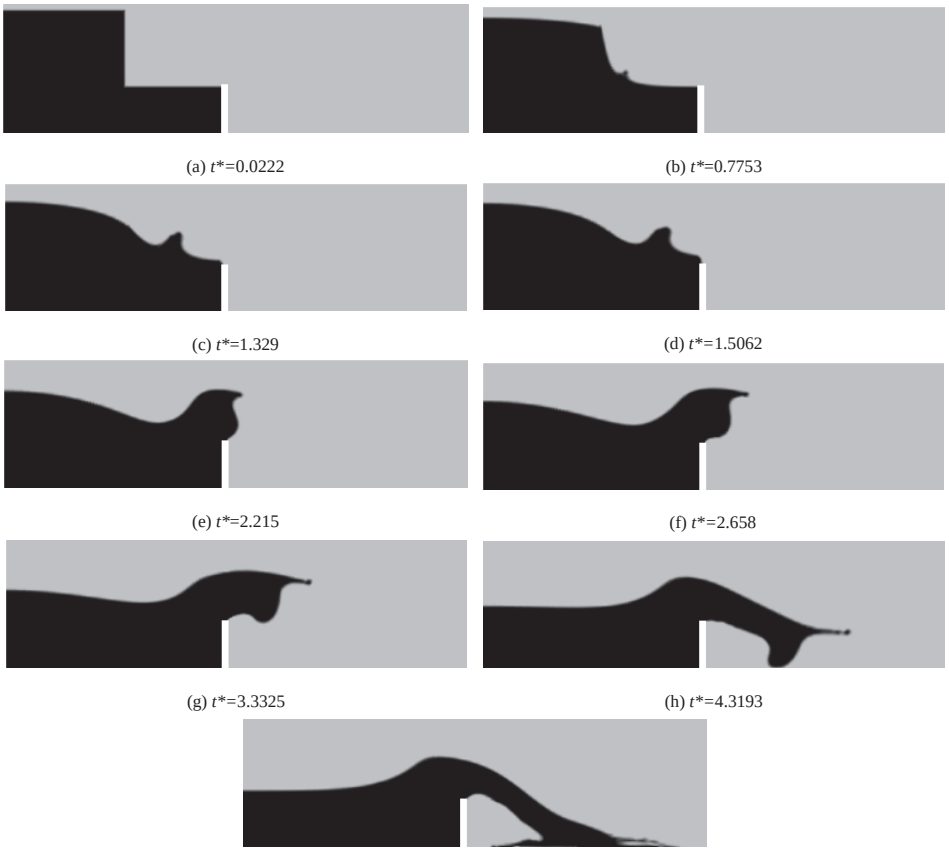

(a) t^*=0.0222 (b) t^*=0.7753

(c) t^*=1.329 (d) t^*=1.5062

(e) t^*=2.215 (f) t^*=2.658

(g) t^*=3.3325 (h) t^*=4.3193

(i) t^*=4.873

Figure 11: Dam-break wave overtopping a spur dike

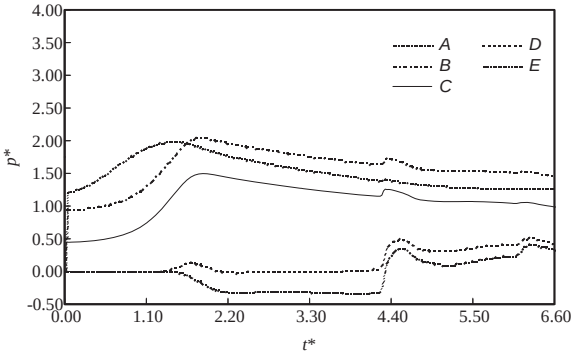

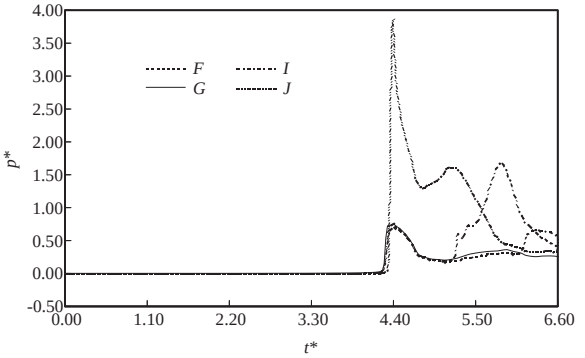

Figure 12: Evolution of the pressure at the control points (Location of the control points shown in Fig. 10)

8 Conclusions

A new dam-break model, in which the CBOS algorithm is used to solve the N-S equations and the PCM is used to capture the moving interface, has been developed.

Dam-break onto a downstream dry bed or wet bed is conducted to verify the present model and it is shown that the present results agree well with the existing solutions or experimental data, so the present model can accurately simulate the moving interface flows.

The complexity of the interface shape occurring in the different stages in the case of dam-break in a confined reservoir, including the gradual formation of the air bubble, can be captured.

For the case of the dam-break wave impact on a spur dike, we successfully reproduce the complex flow process of the dam-break wave over the spur dike, including the generation of dam-break wave, the overtopping the spur dike and the impacting on the downstream seabed. It should be pointed out that:

(i) The pressures, including acting on the downstream seabed and the spur dike, suddenly increase while the dam-break wave over the spur dike impacts on the downstream seabed.

(ii) The pressure at the top of the spur dike decreases even up to negative values, which may be the reason that the centre of curvature of the free surface is below the free surface in [Quecedo, Pastor, Herreros, Merodo, and Zhang (2005)].

Acknowledgement

The author would like to thank the financial support by the National Natural Science Foundation of P. R. China (Grant No. 41072235), the Natural Science Foundation of Liaoning Province of P. R. China (Grant No. 20102006) and the Foundation of Southwest University of Science and Technology of P.R. China (Grant No. 12zx7117).

References

Aliabadi, S.; Tezduyar, T. E. (2000): Stabilized-finite-element/interface capturing technique for parallel computation of unsteady flows with interfaces. *Computer Methods in Applied Mechanics Engineering*, vol. 190, no. 3-4, pp. 243–261.

Boivin, S.; Cayré, F.; Hérard, J. M. (2000): A finite volume method to solve the navier-stokes equations for incompressible flows on unstructured meshes. *International Journal of Thermal Sciences*, vol. 39, pp. 806–825.

Christie, I.; Griffiths, D. F.; Mitchell, A. R.; Zienkiewicz, O. C. (1976): Finite element methods for second order differential equations with significant first derivatives. *International Journal for Numerical Methods in Engineering*, vol. 10, no. 6, pp. 1389–1396.

Donea, J. (1984): A taylor-galerkin method for convective transport problems. *International Journal for Numerical Methods in Engineering*, vol. 20, no. 1, pp. 101–119.

Douglas, J.; Russell, T. F. (1982): Numerical methods for convection-dominated diffusion problems based on combining the method of characteristics with finite element or finite difference procedures. *SIAM Journal on Numerical Analysis*, vol. 19, no. 5, pp. 871–885.

Harlow, F. H.; Welch, J. E. (1965): Numerical calculation of time-dependent viscous incompressible flow of fluid with free surface. *Physics of Fluids*, vol. 8, no. 12, pp. 2182–2189.

Hirt, C. W.; Cook, J. L.; Butler, T. D. (1970): A lagrangian method for calculating the dynamics of an incompressible fluid with free surface. *Journal of Computational Physics*, vol. 5, no. 1, pp. 103–124.

Hirt, C. W.; Nichlos, B. D. (1981): Volume of fluid (vof) method for the dynamics of free boundaries. *Journal of Computational Physics*, vol. 39, no. 1, pp. 201–225.

Hughes, T. J. R.; Franca, L. P.; Hulbert, G. M. (1989): A new finite element formulation for computational fluid dynamics: Viii. the galerkin/least-squares method

for advective-diffusive equations. *Computer Methods in Applied Mechanics and Engineering*, vol. 73, no. 2, pp. 173–189.

Kami, M.; Ossowski, R. L. (2011): On application of the stochastic finite volume method in navier-stokes problems. *Computer Modeling in Engineering and Sciences*, vol. 81, no. 4, pp. 311–334.

Kačeniauskas, A. (2008): Development of efficient interface sharpening procedure for viscous incompressible flows. *Informatica*, vol. 19, no. 4, pp. 487–504.

Kim, M. S.; Lee, W. I. (2003): A new vof-based numerical scheme for the simulation of fluid flow with free surface. part 1: new free surface-tracking algorithm and its verification. *International Journal for Numerical Methods in Fluids*, vol. 42, no. 7, pp. 765–790.

Martin, J. C.; Moyce, W. J. (1952): An experimental study of the collapse of liquid columns on a rigid horizontal plane. *Philosophical Transactions of the Royal Society of London, Series A. Mathematical, Physical and Engineering Sciences*, vol. 244, pp. 312–324.

Masud, A.; Hughes, T. J. R. (1997): A space-time galerkin/least-squares finite element formulation of the navier-stokes equations for moving domain problems. *Computer Methods in Applied Mechanics and Engineering*, vol. 146, no. 1-2, pp. 91–126.

Mohapatra, P. K.; Eswaran, V.; Bhallamudi, S. M. (1999): Two-dimensional analysis of dam-break flow in vertical plane. *Journal of Hydraulic Engineering*, vol. 125, no. 2, pp. 183–192.

Osher, S.; Sethian, J. A. (1988): Fronts propagating with curvature-dependent speed: algorithms based on hamiton-jacobi formulations. *Journal of Computational Physics*, vol. 79, no. 1, pp. 12–49.

Park, I. R.; Kim, K. S.; Kim, J.; Van, S. H. (2012): Numerical investigation of the effects of turbulence intensity on dam-break flows. *Ocean Engineering*, vol. 42, pp. 176–187.

Quecedo, M.; Pastor, M.; Herreros, M. I.; Merodo, J. A. F.; Zhang, Q. F. (2005): Comparison of two mathematical models for solving the dam break problem using the fem method. *Computer Methods Applied Mechanics and Engineering*, vol. 194, no. 36-38, pp. 3984–4005.

Wang, D. G.; Wang, H. J.; Xiong, J. H.; Tham, L. G. (2011): Characteristic-based operator-splitting finite element method for navier-stokes equations. *Science China Technological Sciences*, vol. 54, no. 8, pp. 2157–2166.

Zienkiewicz, O. C.; Nithiarasu, P.; Codina, R.; Vázquez, M.; Ortiz, P. (1999): The characteristic-based-split procedure: an efficient and accurate algorithm for

fluid problems. *International Journal for Numerical Methods in Fluids*, vol. 31, no. 1, pp. 359–392.